Ocean Engineering 238 (2021) 109748

Contents lists available at ScienceDirect

Ocean Engineering

journal homepage: www.elsevier.com/locate/oceaneng

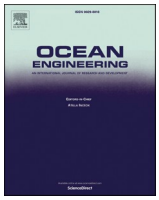

Experimental and numerical determination of the optimum configuration of a parabolic wave extinction system for flumes

U. Izquierdo *, L. Galera-Calero, I. Albaina, A. Vázquez, G.A. Esteban, J.M. Blanco

University of the Basque Country (UPV/EHU) - Faculty of Engineering in Bilbao, Department of Energy Engineering, Plaza Ingeniero Torres Quevedo 1, 48013, Bilbao, Spain

ARTICLE INFO

Keywords:
Reflection coefficient
Iribarren number
Extinction system
Reflection methods
Numerical model validation

ABSTRACT

In this work the phenomenon of the wave reflection has been studied using a self-developed passive extinction system. Twenty one type of waves were generated in the laboratory using a piston-type wave maker. The variation of the reflection coefficient, *Kr*, was studied at several depths (h [m] of 0.3, 0.4, and 0.5), periods ($0.636 < T$ [s] < 1.526), wave heights ($0.010 < H$ [m] < 0.064), slopes ($3 < \alpha$ [°] < 17) and vertical end positions of the extinction system (y_1 [m] and y_2 [m] defined by y_1 [m] and α [°]), covering the linear and non-linear regions of the "Le Méhauté" chart. In parallel, an unsteady numerical model based on the Eulerian multiphase VOF was designed and validated according to the free surface displacement, η_i, and the calculation of the *Kr* values. Both type of validations were successful so this model was used in order to determine *Kr* values at slopes [°] that could not be physically reached by the extinction system. The obtained results allowed to determine the minimum *Kr* values for each set of experiments and finding a useful non-dimensional relationship of $Kr,(h\text{-}y_1)/\lambda$ and *Ir* as a function of the dispersion parameter, *kh*.

1. Introduction

Wave reflection is a phenomenon that may occur in some experimental facilities, such as wave flumes or tanks, when the induced waves interact with any total or partially submerged structure that may be the object of study or the boundary of the fluid domain. As a result of this interaction, new waves with different properties are re-generated, modifying the swell scenario. These types of experimental facilities are widely used to analyse the behaviour of new devices, such as wave energy converters (WECs) (Zhao et al., 2019) or floating structures (Xie et al., 2019) at small scale and representative sea conditions because of their relative low cost and great effectiveness. In the case of WECs, part of the energy of the incident wave will not be absorbed to produce energy, and it will be dissipated by viscous friction in the structure itself, while another fraction will be reflected and/or re-emitted by radiation (in the case of mobile devices). On the other hand, the interaction of extreme waves with offshore wind power structures can put at risk the structural integrity of the anchoring systems, as well as disturb the stability of the wind turbine with significant variations of its optimal orientation with respect to the wind incidence. In this way, the study of wave dissipation and reflection becomes an important issue for the behaviour of different structures subjected to the action of the wave (Esteban Alcalá et al., 2020). Therefore, the wave characteristics need to be perfectly controlled, and consequently the reflection occurring in these facilities must be minimized. The present study analyses the reflection produced by a passive absorption system installed in a wave flume, consisting of a mobile structure with parabolic profile. The adaptive geometry of such system allows optimizing the dissipation of the incident waves according to the specific wave generation.

Wave flumes focus on developing two-dimensional wave trains, so that the infrastructure has to be narrow enough to avoid three-dimensional effects (Izquierdo et al., 2019a; Tutar and Veci, 2016). In parallel, the flume has to be long enough to guarantee fully developed waves. As a whole, the facility can be divided into three different regions: generation, propagation and extinction areas.

The first one or "generation area" is made up of the wave maker and the length of the flume where the wave is directly affected by the inertia of the movement of the paddle. The total length of this area depends on the characteristics of the wave, being required a reference distance of twice the wavelength to consider the wave completely developed (Izquierdo et al., 2019a). Mainly, two types of wave maker present a widespread use in this experimental research field: the "piston-type" (used to generate shallow water-waves, h/λ [-] < 0.05, and

* Corresponding author.
E-mail address: urko.izquierdo@ehu.eus (U. Izquierdo).

https://doi.org/10.1016/j.oceaneng.2021.109748
Received 6 May 2021; Received in revised form 21 July 2021; Accepted 27 August 2021
Available online 1 September 2021
0029-8018/© 2021 The Authors. Published by Elsevier Ltd. This is an open access article under the CC BY license (http://creativecommons.org/licenses/by/4.0/).

Nomenclature

Letters

A_1	amplitude of the primary wave [L]
A_2	amplitude of the secondary wave [L]
AR	aspect ratio [-]
c	waves propagation velocity [$L{\cdot}T^{-1}$]
D	horizontal distance of the extinction system submerged in water [L]
DNS	Direct Numerical Simulations
EWF	experimental wave flume
H	height [L]
H_{max}	wave height in the antinode [L]
H_{min}	wave height in the node [L]
H/λ	wave steepness [-]
h	depth [L]
Ir	Iribarren number [-]
K_r	reflection coefficient [-]
k	wave number [L^{-1}]
k_i	kinetic energy [$L^2{\cdot}T^{-2}$]
R^2	Pearson product moment correlation coefficient [%]
NWF	numerical wave flume
RANS	Reynolds-averaged Navier Stokes
S	stroke [L]
SPH	smoothed particle hydrodynamics
T	period [T]
t	time [T]
VOF	volume of fluid
WECs	wave energy converters
y_1	coordinate for the beginning of the paddle [L]
y_2	coordinate for the end of the paddle [L]

Greek Symbols

Δt	sampling time interval [T]
η_i [m]	free surface displacement [L]
ε	turbulence dissipation rate [$L^2{\cdot}T^{-3}$]
α	slope angle [°]
α_i	volume fraction [-]
ρ_i	density [$M{\cdot}L^{-3}$]
ν_i	dynamic viscosity [$M{\cdot}T^2{\cdot}L^{-1}$]
λ	wavelength [L]

characterized by elliptical trajectories) and the "flap-type" (used to generate deep water-waves, h/λ [-] > 0.5, and characterized by circular trajectories), were h [m] is the depth and λ [m] is the wavelength. While both types are capable to generate waves at intermediate water-depths (0.05 < h/λ [-] < 0.5, and distinguished by elliptical trajectories but not as narrow as shallow waters waves), piston-type wave makers are more suitable to encompass this region (Edinburgh Designs Ltd, 2016; Machado et al., 2018).

The second one, so called "propagation area" consists of the section of the flume where the wave, once fully developed, travels along the flume without suffering any significant modification on its wavelength, period, height or shape. This is the appropriate zone to carry out most of the research activities, such as experiments with floating structures or WECs.

Finally, the "extinction area" that usually consists of a structure where the wave energy is partially (passive systems) or completely (active systems) dissipated. While active wave absorbers can completely neutralize the energy of the incident wave and therefore, avoid the reflection, this is not the case for passive absorbers that are cheaper and easier to install allowing a significant energy absorption by reducing considerably the wave reflection (Ouellet and Datta, 1986). There exists a wide range of different configurations and designs of passive wave absorbers with a permeable (Lim, 2014; Madsen, 1983) or impermeable (Tiedeman et al., 2012) structure. It has been reported that the amount of energy absorption depends on their geometry (Ouellet and Datta, 1986), being the parabolic profile the option that produces a highly effective energy absorption with lower use of the available length of the flume (Ouellet and Datta, 1986; Tiedeman et al., 2012). Hitherto, not any complete study has been reported in the literature that explicitly describes the optimum conditions that minimize the reflection of the waves in a parabolic type passive wave absorber.

Due to the fact that the reflection phenomenon is directly related to the instantaneous characteristics of the wave-structure interaction (i. e. wavelength, period and height), in this study a wide range of monochromatic waves have been studied and the dependence of the reflection phenomenon on the wave parametric domain has been analysed in deep. To determine the reflection and its corresponding coefficient, the incident and reflected waves have to be fully characterized. On the one hand, the incident wave is defined by the movement of the wave maker, which is programmed based on the laboratory wave generation methods (S. A. Hughes, 1993). On the other hand, the reflected wave will depend on the physical properties of the type of absorption system, such as, the profile, position, slope, roughness and elevation. Once the incident wave is partially reflected, it travels towards the opposite direction of the incoming incident waves, generating the wave profile named "resultant wave", being the superposition of the reflected and incident waves. The study of the reflection phenomenon consists of the characterization of the aforementioned wave profiles as a function of the characteristics and position of the absorption system available in the wave flume.

In wave flumes with passive absorption systems, the reflection phenomenon can be characterized by any of the methods available in literature (Frigaard and Brorsen, 1995; Goda and Suzuki, n.d.; Isaacson, 1991; Mansard and Funke, 1980) that define the reflection coefficient, *Kr*, as the ratio of reflected wave height to incident wave height, H [m]. Besides, the coefficient can also be calculated with a spatial method that compares the wave heights in the antinode, H_{max} [m], and the node, H_{min} [m] of the resultant wave from the superposition (Isaacson, 1991), as defined in equation (1):

$$K_r = \frac{H_{max} - H_{min}}{H_{max} + H_{min}} \tag{1}$$

Isaacson (1991) compared different methods for the characterization of the reflection by using fixed probes. Goda & Suzuki (Goda and Suzuki, n.d.) presented a method with two probes and measured the phase-shift between signals and the wave height at each measuring point. They applied a fast Fourier transform method in order to create a flexible and versatile tool that can work with both regular and irregular waves, considering irregular waves as a sum of different regular waves. However, this technique shows some limitations when the spacing between probes is equal to half the wavelength or any of its multiples. In order to verify this method, they compared the results obtained placing the probes at different distances for several runs of two regular waves. Mansard & Funke (Mansard and Funke, 1980) used three probes to measure their phase-shift and the wave height, defining the wave profile in each probe as the summation of the discrete, harmonically related Fourier components. Besides, Isaacson presented another method based on the wave height measurements at three points, excluding the phase-shift measurements because in certain cases they may be inaccurate. Although all the previously described methods are based on the frequency domain, Frigaard & Brorsen (Frigaard and Brorsen, 1995) presented a time-domain based method, which is anyway out of the approach of this study. Moreover (Mora et al., 2018), presented a

mathematical solution for long waves propagating along a slender harbour with a convergent/divergent region, analysing the phenomena that take place in this type of structures and comparing the theoretical formulas with a numerical and analytical models.

In addition, the passive parabolic absorption system can be characterized in terms of reflection coefficient as a function of the Iribarren number, I_r [-] (Iribarren, R., Nogales, 1949):

$$I_r = \frac{\tan(\alpha)}{\sqrt{H/\lambda_0}} \tag{2}$$

where α [°] is the sloping angle (formed by the imaginary straight line that joins the extreme points of the surface and free surface of the water) and λ_0 is the wavelength of the wave developed in deep water with its characteristic period. Battjes (1974) proposed using the I_r number to determine the reflection and dissipation (absorption) of the waves on the breakwater slope, among many other applications. During the last decades, several researchers modified I_r number according to the applications developed, as was mentioned in (Díaz-carrasco et al., 2020).

In addition, Numerical wave flumes (NWF), the computational counterpart of the experimental wave flumes (EWF), are commonly used in order to have a better understanding of any related phenomenon. In the first steps of the design, numerical studies are mainly carried out in 2D developed models that reproduce wave propagation and their interaction with fixed (Viviano et al., 2018) or floating structures (Xie et al., 2019), based on numerical solutions of the fundamental equations corresponding to the fluid motion. For the simulation of wave generation, either for piston or flap-type wave makers, the moving boundary option is used (Altomare et al., 2017). Two main models are used nowadays. The volume of fluid (VOF), a mesh dependant multiphase Eulerian model (Hirt and Nichols, 1981), which has been previously used for the characterization of waves (Izquierdo et al., 2019a), and it is also commonly used to study the performance of floating (Bruinsma et al., 2018) or fixed structures (López et al., 2014). Besides, smoothed particle hydrodynamics (SPH) model has arisen as another interesting option. It is a meshless model that defines the movement and interactions of spherical particles based on Navier-Stokes equations (Higuera et al., 2015). It has been used in the solution of several case studies, such as breaking waves (Dalrymple and Rogers, 2006), green waters (Gómez-Gesteira et al., 2005) or the behaviour of floating bodies under extreme wave conditions (Zhao and Hu, 2012).

2. Aims and methodology

The objective of this study is to provide a clear procedure for the determination of the reflection coefficient, *Kr*, measuring its lowest value for each independent wave generated, based on the detailed study of a self-developed passive extinction system installed in a wave flume of reference. The most important achievement of this work is the characterization of this system, because it is a new concept for energy dissipation that stands out because of its versatility in terms of adaptability to achieve the highest wave energy dissipation rate.

Among the existing methods for the calculation of the Kr value, the one proposed by Mansard & Funke was used aiming to determine the overall position of the absorption system that guarantees the highest wave energy dissipation. The work encompasses the design of a NWF, based on VOF model, further validated through the corresponding experimental tests performed in a particular case study of a EWF. Consequently, the experimental outcomes will be compared according to the method presented by Mansard & Funke, as obtained for the numerical and experimental wave flumes. The NWF was then used to determine the K_r of those constrain positions of the extinction system.

3. Experimental and numerical approach

A significant number of experimental tests and numerical simulations were performed in water at several depths (0.3, 0.4, and 0.5 m) using a piston-type wave maker. Several type of regular waves are analysed in waters of intermediate and deep depths, covering the linear (Airy) and non-linear (Stokes 2nd order) regions of the "Le Méhauté" chart (see Fig. 5), by modifying the period ($0.636 < T$ [s] < 1.526) and the height ($0.010 < H$ [m] < 0.064) respectively. In order to define the inclination of the parabolic structure, the slope α of the imaginary straight line joining the opposite ends has been used in the range of $3 < \alpha$ [°] <17. The time interval elapsed for each experiment ends when the re-reflection occurs in the generation paddle, and it is determined according to the velocity propagation of the waves, *c*. All the data have been processed by using Matlab R2019a (MathWorks, n.d.).

3.1. Experimental wave flume

The EWF is 12.5 m long, 0.60 m wide and 0.7 m high (U. Izquierdo, L. Galera-Calero, I. Albaina, G. A. Esteban, A. Aristondo, 2019). The structure consists of laminated and tempered glass walls supported by a stainless steel platform. The waves are generated through the commercial software Delta-ASDA (V5) (Electronics, 2019) that controls the Delta AC (ASDA-A2 series) servo-drive and servo-motor. The servo-motor is connected to a K series linear actuator (KM60-10 roller screw model), which is attached to a paddle that is partially submerged in water (See Fig. 1). The software allows the paddle to follow a sinusoidal movement or any other higher order movement that turns into a progressive acceleration-deceleration pattern for the generation of waves. Based on the laboratory wave generation methods and applying to a piston-type wave maker (S. A. Hughes, 1993), the movement pattern of the servo drive is specified (position and velocity as a function of time) according to the parameters of the desired wave (λ, T, H and h). Once these parameters are specified, the servo drive engaged the servo motor and the servo motor moves the piston that is attached to the paddle.

The expressions relating the paddle displacement and the generated waves for a piston-type wave maker is defined in equation (3) and the second-order wave board motion in equation (4),

$$m_1 = \frac{H}{S} = \frac{2(\cosh(2kh) - 1)}{\sinh(2kh) + 2kh} \tag{3}$$

$$X_0(t) = A_1 \sin(wt) + A_2 \sin(2wt) \tag{4}$$

$$A_1 = \frac{H}{2m_1} \tag{5}$$

$$A_2 = \frac{H^2}{32h}\left(\frac{3\cosh(kh)}{sinh^3(kh)} - \frac{2}{m_1}\right) \tag{6}$$

$$k = \frac{2\pi}{\lambda} \tag{7}$$

$$w = \frac{2\pi}{T} \tag{8}$$

where, S is the stroke of the paddle displacement, *k* the wave number, *w* the wave frequency and *h* the depth.

Once the desired wave is generated, surface oscillation data are acquired using three resistive-type wave probes of 1.0 m long that were calibrated achieving calibrations errors lower that 0.5%. They are controlled by means of a LABVIEW based program (National Instruments, 2016) able to obtain experimental values of free surface displacement (η_{exp}^{i}) as a function of time (t, with a sampling time interval of $\Delta t = 3$ ms) for each wave probe. The main properties of the equipment described above are detailed in (Izquierdo et al., 2019b). The first probe position is set at 6.0 m from the wave generating position and the distance between consecutive probes is stablished according to the criteria described in (Goda and Suzuki, n.d.) depending on each wave's

Fig. 1. Top: Overall view of the EWF of the Energy Engineering Department (UPV/EHU). Bottom: (left) Resistive-type wave probes and (right) piston-type wave generation system.

parameters. The extinction region consists of a self-designed passive absorption system, with a parabolic solid area of 1.5 m length that can be adjusted manually by modifying the height (C), the slope (B) or the elevation (D) through precision screws, as depicted below in Fig. 2. The parabola that defines the shape of the surface of the self-designed extinction system is based on (Ouellet and Datta, 1986), and it corresponds to the following equation:

$$y[mm] = 200 + 0.023x - 9{\cdot}10^{-5}x^2 \tag{9}$$

The design of this extinction system permits to be adapted, depending on the depth, the type of wave or the type of study being carried out in the flume, in height and angle. In addition, the surface, which is completely smooth for this study, could also be substituted by any other type of surface such as rough or perforated.

3.2. Numerical wave flume

3.2.1. Governing equations

Conservation equations, most known as Navier-Stokes equations, are used to define the behaviour of Newtonian fluids. These equations are the mass conservation (10) and the momentum conservation (11) equations that in an incompressible fluid can be defined as:

$$\nabla \vec{U}_i = 0 \tag{10}$$

$$\frac{\partial \vec{U}_i}{\partial t} + \left(\vec{U}_i \cdot \nabla\right)\vec{U}_i = -\frac{1}{\rho}\nabla p + \nu\nabla^2\vec{U}_i + \vec{g} \tag{11}$$

where $\vec{U}_i$ is the velocity of the flow in each of the dimensions, being $i =$ 1,2,3, ρ the density of the fluid, p the pressure, ν the dynamic viscosity, and $\vec{g}$ the gravity vector. These equations can define all the states of a flow, from laminar to turbulent states, where a lot of eddies of different sizes appear, due to the energy cascade effect. This defines the energy transmission from larger eddies to smaller ones, repeatedly, until the smallest eddies are dissipated by viscous effects or heat dissipation. The direct application of these equations, known as Direct Numerical Simulations (DNS), is possible. However, this approach has a high computational cost due to the calculation of all turbulent scales. Besides, simplified approaches have been used for engineering applications throughout the last decades with great accuracy. The most common approach is to apply the Reynolds decomposition to the Navier-Stokes equation (12). This decomposition focusses on the mean and fluctuating values of the fluid velocity in a certain point.

$$\vec{u}_i(x,t) = \overline{U}_i(x) + u_i'(x,t) \tag{12}$$

where $\vec{u}_i$ is the velocity in a certain point in each instant time, $\overline{U}_i(x)$ is the mean value of the velocity in that point and $u_i'(x,t)$are the fluctuations of the velocity in space and time. Thus, the application of this decomposition generates the Reynolds-Averaged Navier-Stokes (RANS) equations. This process introduces new components to the equations, such as the Reynolds-stress tensors (τ_{ij}) in the momentum equation. The mass and momentum equations for RANS are:

$$\nabla \overline{U}_i = 0 \tag{13}$$

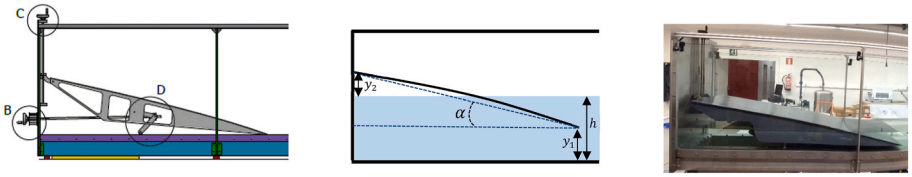

Fig. 2. Detail of the self-designed extinction system (left) and its real picture in the experimental facility (right).

$$\frac{\partial \overline{U_i}}{\partial t} + \overline{U_j}\frac{\partial \overline{U_i}}{\partial x_j} = \frac{1}{\rho}\frac{\partial}{\partial x_j}\left(-p\delta_{ij} + 2\mu S_{ij} + \tau_{ij}\right) + g \tag{14}$$

where $\overline{U_j}$ is the time-averaged fluid flow, ρ is the density, p is the pressure, μ is the viscosity, i,j equals to 1, 2, and 3, which are the three spatial dimensions, δ_{ij} is the Kronecker function, S_{ij} is the viscosity tensor and τ_{ij} is the Reynolds Stresses.

$$S_{ij} = \frac{1}{2}\left(\frac{\partial \overline{U_i}}{\partial x_j} + \frac{\partial \overline{U_j}}{\partial x_i}\right) \tag{15}$$

$$\tau_{ij} = -\rho\overline{u_i' u_j'} \tag{16}$$

For this study, STAR-CCM + software has been used for the RANS approach that we imposed into the numerical simulations. The fluctuation Reynolds-Stresses are modelled with the Boussinesq hypothesis:

$$\tau_{ij} = \mu_t\left(\frac{\partial \overline{U}_i}{\partial x_j} + \frac{\partial \overline{U}_j}{\partial x_i}\right) - \frac{2}{3}\left(\rho k_t + \mu_t\frac{\partial \overline{U}_i}{\partial x_i}\right)\delta_{ij} \tag{17}$$

where μ_t is the eddy viscosity and k_t the turbulent kinetic energy. This model, inserts two new variables to the Navier-Stokes equations, generating an open system. Thereby, more equations are needed to close the system. To do that, a two-equation turbulence model is inserted for this aim. The model is the Low Re k-ε model.

$$\rho\frac{\partial k_t}{\partial t} + \rho\overline{U}_j\frac{\partial k_t}{\partial x_j} = S_{ij}\frac{\partial \overline{U}_i}{\partial x_j} - \rho\varepsilon_t + \frac{\partial}{\partial x_j}\left[\left(\mu + \frac{\mu_t}{\sigma_k}\right)\frac{\partial k_t}{\partial x_j}\right] \tag{18}$$

$$\rho\rho\frac{\partial \varepsilon_t}{\partial t} + \rho\overline{U}_j\frac{\partial \varepsilon_t}{\partial x_j} = C_{\varepsilon_1}\frac{\varepsilon_t}{k_t} + S_{ij}\frac{\partial \overline{U}_i}{\partial x_j} - C_{\varepsilon_2}\rho\frac{\varepsilon_t^2}{k_t} + \frac{\partial}{\partial x_j}\left[\left(\mu + \frac{\mu_t}{\sigma_\varepsilon}\right)\frac{\partial \varepsilon_t}{\partial x_j}\right] \tag{19}$$

$$\mu_t = \frac{\rho C_\mu k_t^2}{\varepsilon_t} \tag{20}$$

where ε_t is the energy dissipation rate, and $C_{\varepsilon 1}$, $C_{\varepsilon 2}$, C_μ, σ_k, and σ_ε are model coefficients. RANS equations are used with a second order temporal discretization. Eulerian multiphase VOF unsteady model is implemented to define both fluids, taken also into account the effects of gravity and surface tension respectively (Galera-calero and Izquierdo, 2020; Hirt and Nichols, 1981). The volume fraction can be defined as the percentage of the cell volume that one fluid occupies, which transport equation can be defined as:

$$\frac{\partial \alpha_i}{\partial t} + \nabla\left(\alpha_i \vec{U}_i\right) = 0 \tag{21}$$

where α_i is the volume fraction, t the time and U_i is the flow velocity vector. The free surface orientation is defined by determining in which direction the value varies more rapidly, which defines the normal direction of the free surface in each cell. The computational results were recorded by defining the corresponding vertical planes for each computational wave probe. Results in terms of free surface displacement ($\eta_{com}{}^i$) as a function of time were acquired in each time-step of the simulation. The properties of each fluid are defined as follows (Guide, 2015):

$$\rho = \sum_i \alpha_i\rho_i \tag{22}$$

$$\mu = \sum_i \alpha_i\nu_i \tag{23}$$

α_i, ρ_i and ν_i are calculated for each cell all over the computational domain. The k-ε provides a general description of turbulence by means of two transport equations: one for the kinetic energy, k_i, and another for the turbulence dissipation rate, ε (Windt et al., 2018). Besides, previous work has been developed with this turbulence model achieving successful validation results (Izquierdo et al., 2019a). It was selected because the two-layer approach is valid for low and high wall y^+ values providing a better definition of the near wall treatment.

3.2.2. Definition of the geometry and movement of the wave generator

A 2D Numerical Wave Flume (NWF) containing two phases, water and surrounding air, has been built(Galera-Calero et al., 2020). The NWF is 12.0 m length and 0.7 m high. When compared to the EWF, for the NWF the volume of water behind the wave maker (0.5 m length) is neglected because it is considered as a solid mobile wall without water movement between both volumes. The solid mobile wall reproduces accurately the behaviour of the wave maker with a morphing grid-velocity condition, which allows defining its velocity variation during each cycle in the corresponding simulation (see Fig. 3). The movement of the paddle depends on the wave to be generated, being linear (Airy) and non-linear (Stokes 2nd order) waves the last modelled in this study. This implies the use of motion equations that control the displacement of the paddle according to each specific wave to be generated. These equations are obtained from the theory of the wave maker (S. A. Hughes, 1993) and are set up in the software that controls the paddle.

$$x(t) = -A\cdot\cos\left(\frac{2\pi}{T}\cdot t\right) \tag{24}$$

where A is the amplitude of the curve, which is equal to half of a Stroke ($S/2$), being T the period and t the time interval for the linear wave. Deriving equation (24), the mathematical equation for linear waves (25) that defines the velocity of the paddle as a function of time is obtained:

$$v(t) = \frac{2A}{T}\pi\cdot\sin\left(\frac{2\pi}{T}\cdot t\right) \tag{25}$$

To reproduce non-linear waves, the movement equation of the paddle is defined as follows:

$$x(t) = -A_1\cdot\cos\left(\frac{2\pi}{T}\cdot t\right) + A_2\cdot\cos\left(\frac{4\pi}{T}\cdot t\right) \tag{26}$$

where A_1 is the amplitude of the primary wave, A_2 the amplitude of the secondary wave, T is the period and t is the time dependant variable for the non-linear wave. Deriving equation (26), the corresponding velocity of the paddle is obtained (27):

$$v(t) = \frac{2A_1}{T}\pi\cdot\sin\left(\frac{2\pi}{T}\cdot t\right) - \frac{4A_2}{T}\pi\sin\left(\frac{4\pi}{T}\cdot t\right) \tag{27}$$

Fig. 3 shows the general scheme of the boundaries of the computational domain. The top wall is defined as a pressure outlet, which allows the air to move throughout freely, while the bottom is defined as a wall. Both have a boundary constraint plane to allow the movement of the wave maker, which is defined as a moving wall. All the boundaries defined as walls have a non-slip condition to reproduce the same effect that the physical boundaries have in the experimental flume, being these boundaries the end wall, the bottom and the extinction system. This

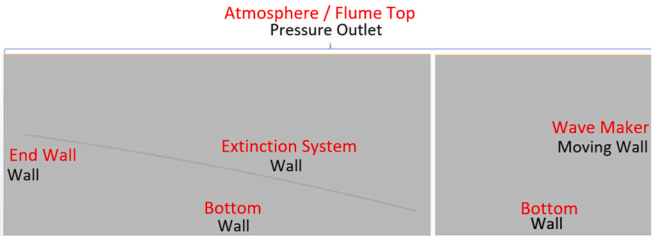

Fig. 3. Conditions imposed in the different boundaries of the numerical domain.

system is numerically reproduced by two parabolic walls (both fixed and with non-slip conditions). The position of the parabolic walls defines the desired angle of the extinction system, which must be specified in each experiment, being the angle defined by the straight line that joins the highest and lowest point of the extinction system and the horizontal direction.

3.2.3. Mesh definition

The mesh has been optimized through a mesh sensitivity analysis aiming for reducing the computational cost but achieving the most accurate definition of the free surface displacement. This has been carried out by defining several areas in the domain: (1) the area where the fluid is only air, (2) the area where a free surface displacement is studied, (3) the area where there is always water, and two areas of special interest, the generation paddle and the extinction beach respectively. All of these areas can be observed in detail in Fig. 4:

While the area in which the fluid is always air (1) the base cell size is a square of 20 cm, the area closer to the free surface is meshed with significantly smaller cells, adjusting their size to the wave height and wavelength. For this last, since the propagation of the wave is much faster than the proper free surface elevation (the horizontal displacement is faster than the vertical one), quadrilateral cells have been used with an aspect ratio (AR [-]) of 4.0, being quadrilateral cells of 1.5 mm $\times$ 6.0 mm (length x height). Besides, a growth factor of 1.3 is imposed in the extinction system surface to achieve a good definition of the wave breaking. For the area where there is always water (3), cells with an AR $=$ 2.0 are used, being quadrilateral cells of 2.0 mm $\times$ 4.0 mm (length x height). Finally, prism layers were generated for the areas of the generation paddle and the extinction system respectively. For them, 20 and 13 prism layers with a stretching coefficient of 1.2 and 1.3, and a total thickness of 3.0 cm and 1.0 cm respectively were generated. The total amount of cells, for the lowest wave height tested in each depth, is 637641 for h $=$ 0.3 m, 727266 for h $=$ 0.4 m and 610715 for h $=$ 0.5 m. This allows simulating 30 s in approximately 10 h using a time step of 0.001 s and 5 inner iterations in a DELL precision 7920, with 24 Xeon cores and RAM of 32 Gb workstation. The cell size was calculated based on the Courant number limitation, being always lower than 0.40 for the second order waves and lower than 0.87 for the first order waves.

4. Experimental campaign

The experimental tests were defined considering the length of the wave flume and the capacity of the servo-motor. In addition, for all the experiments the maximum and minimum wave heights were delimited in order to avoid the trough passing under the extinction system or the peak to overflow it. Each wave was defined as follows: first, the depth of the experiment was decided, then, based on the non-dimensional "Le Méhauté" chart (see next Fig. 5), a specific value of the *x*-axis coordinate was selected to define the *T*. Next, the value of *H* was calculated from the corresponding value of the *y*-axis coordinate.

Subsequently, the wavelength was obtained through the wave dispersion relation, given by equation (27):

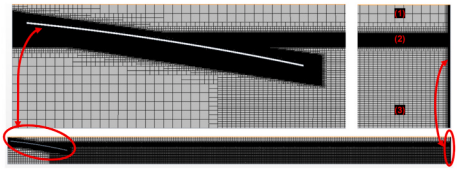

Fig. 4. Top: Amplified areas of special interest: focus on the prism layers around the wave maker (left) and The different areas of the mesh: (1) air, (2) area where a free surface displacement is measured, (3) water (right). Bottom: overall view of the NWF mesh.

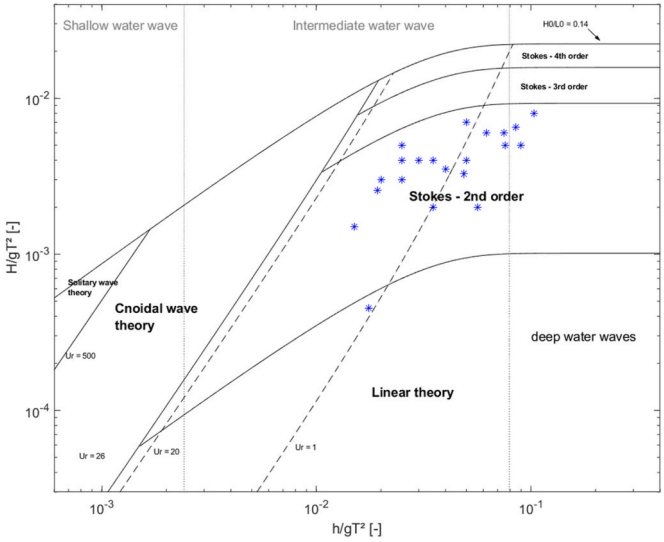

Fig. 5. Le Méhauté chart, indicating the validity range of various wave theories, in which the generated waves are depicted.

$$\lambda = \frac{gT^2}{2\pi} tanh\left(\frac{2\pi h}{\lambda}\right) \tag{27b}$$

and finally, the movement of the paddle was specified as described in equations (3) and (4). Thereby, 21 waves were theoretically defined as was previously mentioned, covering the linear and non-linear regions in a wide range of *T*, *H* and λ as shown in Table 1.

The modification of α would allow obtaining a trend and determining the lowest *Kr* value (corresponding to the highest wave energy absorption). For each experiment, α of the extinction system was set by modifying the vertical position of the opposite ends: the coordinate for the beginning of the paddle y_1, that is always submerged, and the coordinate for the end of the paddle y_2, that is always above the free surface. The value α was increased for each experiment at intervals of 2° for the ranges specified in the last column of Table 1. Moreover, it was also taken into account the horizontal displacement of the extinction system in order to define the mesh for each *h* and α. As it is discussed in Section *4, Results and discussion*, for some waves it was not possible to

Table 1
Main parameters of the theoretically defined waves for three different depths. I: intermediate water-waves, D: deep water-waves, S: Stokes and A: Airy.

h [m]	Wave	*T* [s]	*H* [m]	λ [m]	*h*/λ [-]	α [°]
0.3	1, I-S	0.64	0.020	0.63	0.476	3–15
	2, I-S	0.79	0.020	0.94	0.319	
	3, I-S	0.93	0.034	1.24	0.242	
	4, I-S	1.01	0.040	1.39	0.216	
	5, I-S	1.11	0.060	1.59	0.189	
	6, I-S	1.26	0.040	1.89	0.159	
	7, I-S	1.43	0.030	2.21	0.136	
0.4	8, D-S	0.69	0.031	0.75	0.533	5–17
	9, I-S	0.81	0.039	1.01	0.396	
	10, I-S	0.90	0.040	1.23	0.325	
	11, I-S	1.01	0.035	1.49	0.268	
	12, I-S	1.28	0.064	2.11	0.190	
	13, I-S	1.43	0.060	2.46	0.163	
	14, I-A	1.53	0.010	2.67	0.150	
0.5	15, D-S	0.70	0.039	0.77	0.649	5–17
	16, D-S	0.75	0.028	0.88	0.568	
	17, I-S	0.82	0.040	1.05	0.476	
	18, I-S	0.95	0.018	1.38	0.362	
	19, I-S	1.01	0.040	1.54	0.325	
	20, I-S	1.21	0.029	2.07	0.242	
	21, I-S	1.43	0.060	2.64	0.189	

experimentally determine the lowest *Kr* value because of design constraints that make impossible setting the extinction systems in limiting positions so that the minimum value would be achieved. Once the validation of the computational model was carried out, the *Kr* values of those positions were determined.

4.1. Validation of the computational model

A triple comparative between theoretical, experimental and computational results in terms of *T*, *H* and λ was carried out in order to validate the computational model, ensuring the reliability of the calculated *Kr* values. The free surface displacement of the experimental and computationally acquired signals, $\eta_{com}{}^{i}$ and $\eta_{exp}{}^{i}$, provides information about how accurate the computational model reproduces the waves generated in the flume. For both, experimental and computational experiments, the phase shift was measured between the signals acquired by two consecutive probes, which also permitted to calculate the wave propagation velocity, c [m/s]. *Fig. 6* contains the signal information during the time interval corresponding a complete experiment (generation, propagation and reflection) for a particular wave measured by one of the probes. The Wave 11 is selected because it represents approximately the average values of the analysed parameters (*h*, *T*, *H* and λ).

The parameters of the experimental and numerically generated waves were calculated by using Matlab R2019a to fit their free surface signal to the corresponding wave theory equations (linear or non-linear). For the case of Wave11 represented in Fig. 6, the experimental and computational data ranged between $8.2 < t\ [s] < 13.5$, the ones corresponding to the propagation period, were fitted to a non-linear wave equation. During this time interval, the wave is considered fully developed and therefore, it is not yet influenced by the reflection. Besides, the data used for the calculation of the *Kr* value are inside the time interval $15.5 < t\ [s] < 17.9$. From this, the signal acquired by the wave probes would correspond to a re-reflected wave train and therefore, the data would not be valid for this study.

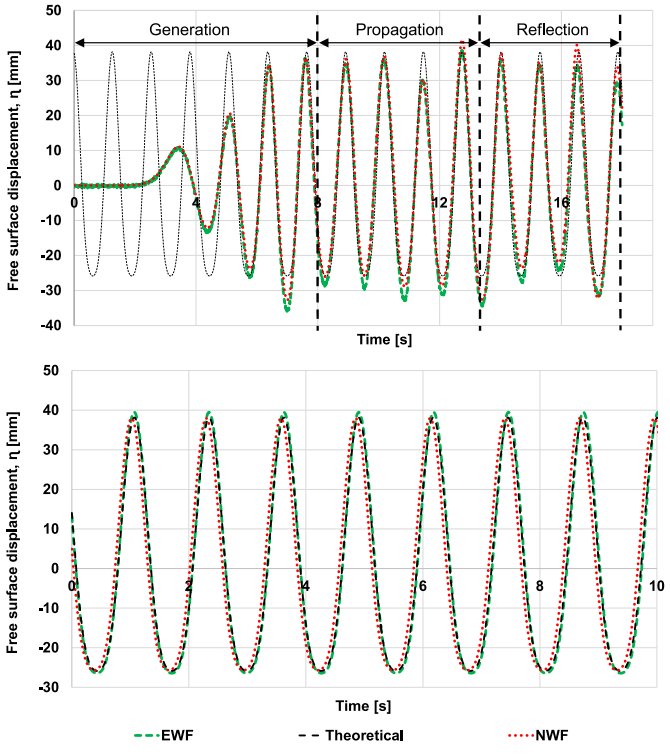

Fig. 6. Top: Comparative of the experimental and numerical free surface displacement signals, with the theoretical parameters of Wave 11, for a complete experiment. Bottom: Comparison of theoretical parameters of Wave 11 with experimental and numerically obtained wave parameter.

The fittings carried out for both, experimental and computational signals, provided the corresponding results in terms of *T*, *H* and λ as well as the value of the square of Pearson's product-moment correlation coefficient, R^2. On the one hand, the average among all the experiments carried out for the calculated R^2 is 97.6% and the comparison between experimental and computational signals fitting provided a R^2 value higher than 99.5% (see Fig. 7). On the other hand, the measured *T*, *H* and λ were compared with the analytical values given by the wave theory in order to calculate the corresponding relative errors. For almost all the experiments errors below 3% were measured and for some punctual experiments below 5%. This demonstrated an appropriate operation of all the components of the wave flume and a successful design of the numerical model.

Finally, the validation experiments aimed to prove the validity of the model by comparing results for several *h*, *T*, α and vertical positions of the extinction system (y_1, y_2). Thus, two specific positions were selected -with completely different coordinates-, two angles -for which minimum *Kr* values were experimentally calculated- and, for both cases, most of the waves reproduced in the laboratory at those conditions. Fig. 8 shows a comparative test between experimental and numerical results in terms of the *Kr* value, both calculated by the method of Mansard & Funke:

Both, the tendency and the *Kr* values are very close to each other. Taking into account that this coefficient is a mathematical division of values of which two of them are obtained after 17 s, it can be affirmed that the results reflect successful computational simulations. This computational model is therefore valid for the cases in which the trend followed was not completely clear or, it seemed that the minimum of the *Kr* values was not reached. As it was previously commented, this happened for the experiments carried out at $h = 0.5$ m, so that these specific experiments were numerically reproduced, and the results showed that none of the computational results offered a new minimum *Kr* value.

5. Results and discussion

Results have been analysed to determine the minimum *Kr* value as a function of a non-dimensional parameter $(h\text{-}y_1)/\lambda$, defined by the relation between the effective vertical distance of the extinction system, $(h\text{-}y_1)$, with the wavelength, λ. This parameter defines the relative length of the liquid depth that is covered by the vertical projection of the extinction system $(h\text{-}y_1)$, with respect to the size of the wave given by the wavelength, λ. A higher value of this parameter will lead to a greater interaction of the extinction system with the larger orbitals of the fluid particles of the wave (i. e. the ones closer to the free surface). On the contrary, a smaller bottom gap below the extinction system, would allow the wave passing through and reflect directly on the vertical wall end of the flume. In *Fig. 9* the results obtained at $h = 0.3$ m are shown, as

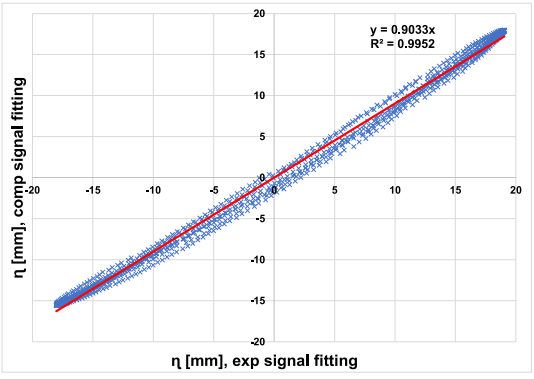

Fig. 7. Comparison between the computational and experimental signals fittings for the Wave 11 during the time interval of the experiment.

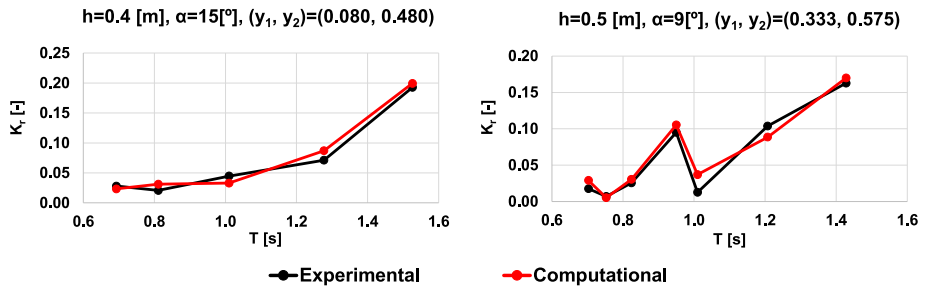

Fig. 8. Comparative between experimental and numerical results of two specific positions, angles and depths for the waves 8, 9, 11, 12, 14, 15, 16, 17, 18, 19, 20, 21.

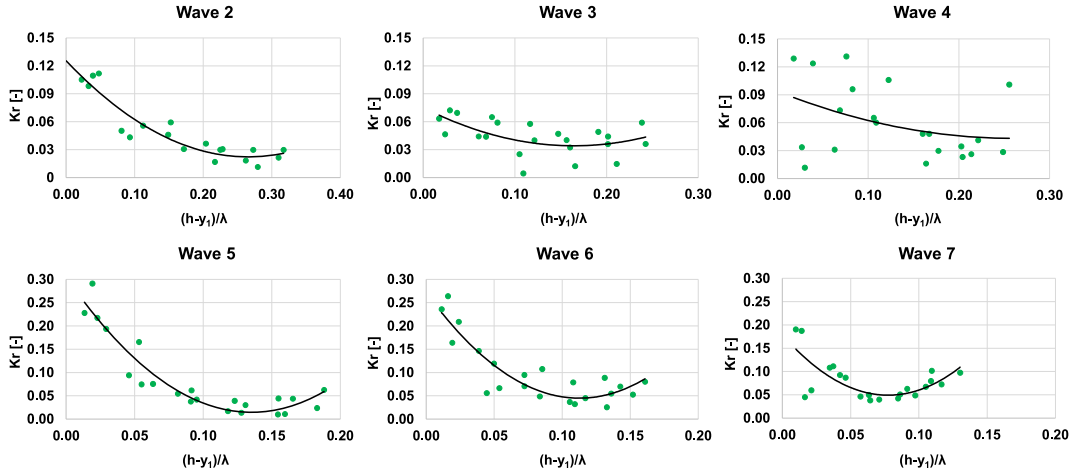

Fig. 9. Results of the Kr obtained at h = 0.3 m (waves 2 to 7 of Table 1) as a function of (h-y1)/λ.

calculated by the Mansard & Funke method.

In this Fig. 9, the corresponding fittings to a second order polynomial equation have been represented in order to analyse the trend of the *Kr* value and determine the influence of the submersion of the extinction system. For all the waves generated, at low $(h\text{-}y_1)/\lambda$ values the highest *Kr* values were calculated and, once the minimum values were achieved at intermediate $(h\text{-}y_1)/\lambda$ values, the *Kr* increases again when the submersion of the paddle was the minimum. This reveals that the highest energy dissipation rate is never obtained when the extinction system is completely submerged. In a similar way, the same approach has been carried out for the experiments at $h = 0.4$ and 0.5 m, achieving same conclusions. However, the increase of the *Kr* value is also related with the *Ir* number. Then, analogous trends can be also obtained as a function of *Ir* number, which is shown in Fig. 10 for waves generated at $h = 0.5$ m.

The *Ir* number, defined in equation (2), depends on the sloping angle and the wavelength of the wave developed in deep water. The trends obtained in this Fig. 10 are very similar to the ones shown in Fig. 9: highest energy dissipation rate is obtained when the extinction system is partially submerged. In general, when *Kr* is represented as a function of $h\text{-}y_1$, $(h\text{-}y_1)/\lambda$ or *Ir*, analogous tendencies are obtained, or the contrary ones when represented against y_1. However, the increasing *Kr* values can also be explained according to the breaking behaviour of waves,

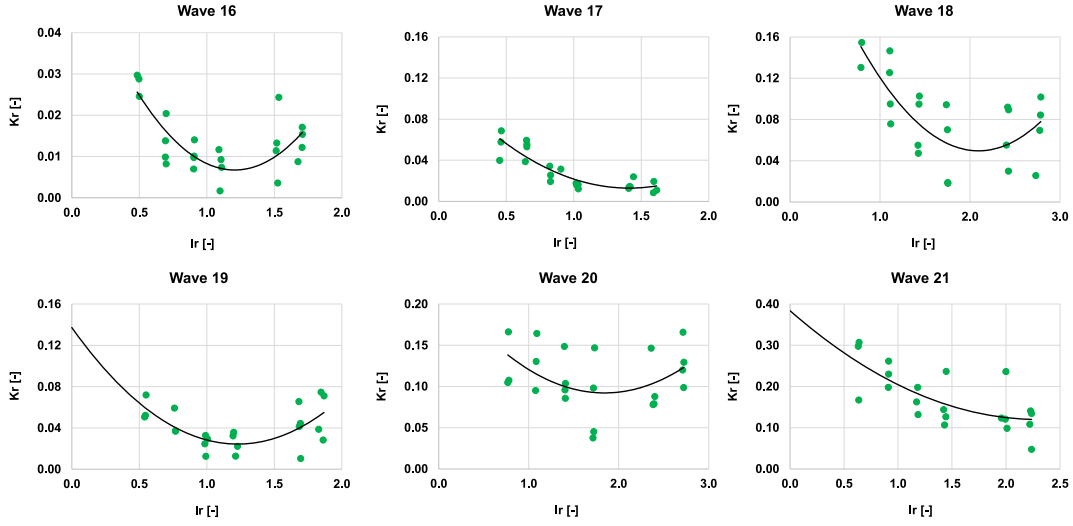

Fig. 10. Results of the Kr obtained at h = 0.5 m (waves 16 to 21 of Table 1) as a function of Ir.

because the *Ir* number has been used to define different types of breaking, according to the following intervals: Ir < 0.5 "spilling", 0.5 < Ir < 3.3 "plunging" and Ir > 3.3 "collapsing/surging" (Battjes, 1974). Based on this classification, the waves generated in this work corresponds to the spilling and plunging breakings. The higher the value of the *Ir* number the less dissipative and more reflective the type of wave breaking becomes. In the extinction system, the enhancement of spilling far from surging mode should be pursued in order to minimize the value of the reflection coefficient. This makes the self-designed system a very useful and effective extinction system to minimize the reflection of any generated wave.

In the next Fig. 11 a comparison between spilling and plunging type of breaking can be observed, as simulated for Wave 4 (*Ir* = 0.32, spilling) and Wave 7 (*Ir* = 1.97, plunging). The captures show clearly the evolution of the waves when breaking. While Wave 4 travels through a large part of the extinction system, smoothly and with enough time until the next incoming wave interacts, Wave 7 breaks abruptly and in a short part of the extinction system.

The next Fig. 12 shows the relationship between *Kr* and $(h\text{-}y_1)/\lambda$ divided in several intervals of *Ir*. The first interval corresponds to the spilling type of breaking, and the others are four intervals comprehended into the plunging type of breaking.

Fig. 12 comprises all the experiments carried out with the 21 different waves. Several intervals were defined for the plunging type breaking in order to reduce the dispersion of the results when shown with their corresponding fittings to a potential equation. At low $(h\text{-}y_1)/\lambda$ values the highest *Kr* values were calculated and, according to this type of breaking, the lowest *Kr* values were calculated for spilling. It can also be appreciated the influence of the submerged part of the extinction system for the energy dissipation, decreasing at higher $(h\text{-}y_1)/\lambda$ values. In this figure, it can also be clearly appreciated the increase of *Kr* values at a constant $(h\text{-}y_1)/\lambda$, when increasing *Ir* number values. In the contrary way, Fig. 13 represents the influence of the *Ir* number, having divided several intervals of $(h\text{-}y_1)/\lambda$. Here, it can more clearly be observed that *Kr* values increase at increasing *Ir* numbers. However, it is more evident the successful design of the extinction system because of the smooth increase of the *Kr* values at increasing *Ir* number, when $(h\text{-}y_1)/\lambda$ value is high.

In addition to the previous results, the corresponding correlation between the minimum calculated *Kr* values, $(h\text{-}y_1)/\lambda$ and *Ir* number was obtained as a function of the dispersion parameter, *kh*. This triple approach provides a universal relationship in terms of these three parameters aiming to achieve the minimum *Kr* value.

Fig. 14 (left) shows how the lower relative period and wavelength of the wave (higher *kh*) the higher the possibility to dissipate the wave and minimize the reflection coefficient by an optimized position of the parabolic extinction system. In addition, Fig. 14 (right) defines the optimum configuration to get such a minimum value of *Kr* in a dimensionless way in terms of the surf parameter *Ir* and the "vertical coverage" $(h\text{-}y_1)/\lambda$. It can be noticed that relative longer waves need a shorter vertical coverage of the wave by the parabolic system and a slightly higher value of the surf parameter *Ir* to get a minimum reflection coefficient.

The particular system used for the wave energy dissipation complicated the possibility of comparing results with other similar systems

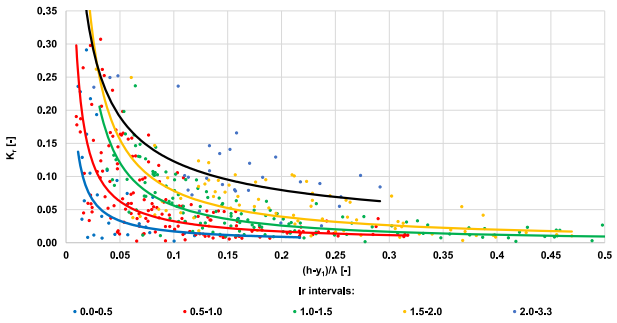

Fig. 12. *Kr results as a function of $(h\text{-}y_1)/\lambda$, divided in several intervals of the Ir number, for all the experiments carried out.*

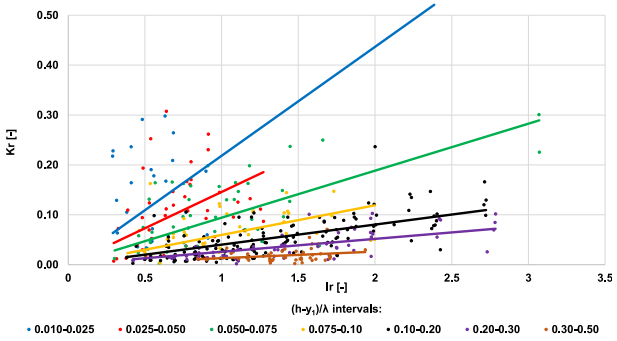

Fig. 13. *Kr results as a function of Ir, divided in several intervals of $(h\text{-}y_1)/\lambda$, for all the experiments carried out.*

because most of them are attached to the bottom of the flume and were carried out mostly in deep water-waves (Battjes, 1974; Hodaei et al., 2016; Ish M and Raju, 2004; Ouellet and Datta, 1986; Puspita et al., 2019). While all of those systems are completely static, the extinction system presented here allows obtaining various sloping angles and vertical positions, which seems to be the key factor to minimize the reflection along the flume. Nonetheless, the results have been compared with those obtained in other models reported in specialized literature as shown in Table 2:

The results obtained in the present work have been compared with those of (Puspita et al., 2019), (Hodaei et al., 2016), and (Puspita et al., 2020). It is worth noting the benefit of using a parabolic extinction system with smaller values of reflection coefficient in comparison to the more traditional plane inclined plate. In the present piece of research a methodology to optimise the geometric location of the parabolic profile in relation of the properties of the incident wave has been developed. As a consequence, minimum values of the reflection coefficient below the reference of *Kr* = 0.08 have been achieved, which implies a significant comparative improvement within the available passive extinction methods. In addition, focusing on characteristics of the absorption systems of the literature, it seems possible to continue reducing the reflection along the flume by perforating the surface of the absorption system, which will be considered in future work.

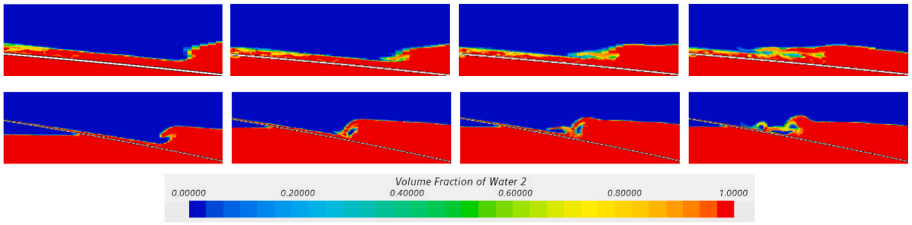

Fig. 11. *Captures corresponding to the extinction system, showing the wave breaking for Wave 4 (top: Ir = 0.32, spilling) and Wave 7 (bottom: Ir = 1.97, plunging).*

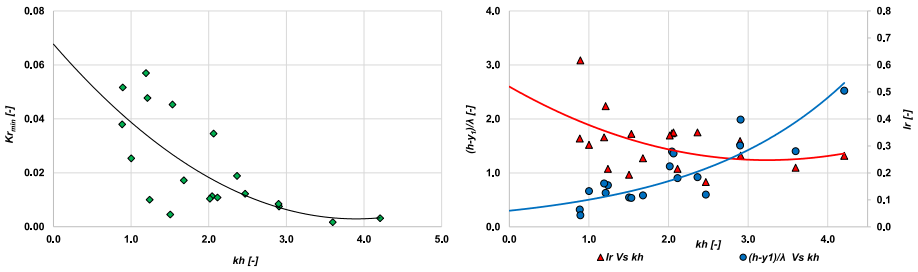

Fig. 14. Minimum *Kr values calculated among all the* y_1 *and* α *combination for the 21 waves generated.*

Table 2
Results comparison with similar extinction systems.

Authors	Wave flume [m] (Length x width x height)	Absorption system	H [m]	T [s]	K_r [-]
Izquierdo et al.	12.5 × 0.5 x 0.7	Parabolic profile	0.01–0.064	0.64–1.53	~0.08
Rostaminia and Chegini (2008)	32.5 × 5.5 x 1	Single perforated flat plate	–	–	~0.26
Hodaei et al.	108 × 3 x 2.5	Parabolic profile	0.03–0.25	1.08–1.52	~0.09
Puspita et al.	15 × 0.3 x 0.45	Plane plate	0.04–0.06	0.6–1.3	Plunging >0.1 Surging >0.2

6. Conclusions

The phenomenon of the reflection has been studied using a self-developed passive extinction system installed in a wave flume of 12.5 m long, 0.60 m wide and 0.7 m high. The slope of this absorption system can be modified as well as its vertical end position which increased the possibility to find the optimal position for the wave energy dissipation. A significant number of experimental tests were reproduced in the laboratory by means of a piston-type wave maker. Several depths (h of 0.3, 0.4, and 0.5 m respectively), periods ($0.636 < T$ [s] < 1.526), wave heights ($0.010 < H$ [m] < 0.064), slopes ($3 < \alpha$ [°] < 17) and vertical positions ($0.005 < y_1$ [m] < 0.279 at $h = 0.3$ m, $0.008 < y_1$ [m] < 0.385 at $h = 0.4$ m, $0.098 < y_1$ [m] < 0.465 at $h = 0.5$ m and y_2 [m] defined by y_1 [m] and α [°]) of the extinction system, covering the linear (Airy) and non-linear (Stokes 2nd order) regions of the "Le Méhauté" chart, were studied.

A computational model based on the Eulerian multiphase VOF unsteady model was designed to reflect through simulations any of the conditions that can be reproduced in the experimental wave flume. A successful validation of the computational model was carried out, being the simulations checked by two different ways: on the one hand, a validation based on the free surface displacement, η_i (by comparing the theoretical, experimental, and numerical signals), and on the other hand, a validation based on the calculation of the *Kr* values was carried out. Both ways were successfully achieved because the error was negligible. In addition, this model was used in order to determine *Kr* values at slopes that could not be physically reached by the extinction system, which was very useful to determine certain trends at $h = 0.5$ m.

The calculated *Kr* experimental results were analysed in terms of a non-dimensional $(h\text{-}y_1)/\lambda$ parameter, which relates the energy dissipation with the part of the extinction system that is submerged. The main conclusion achieved is that the maximum energy dissipation strongly depends on its vertical position. In addition, the experimental results have also been analysed with respect to the *Ir* number. In this case, the relation of the type of breaking with the energy dissipation have been confirmed. However, it has also been valid to confirm that the highest energy dissipation rate is never obtained when the extinction system is attached to the bottom of the flume, being needed to rise it to minimize the reflection.

Furthermore, the minimum *Kr* values were extracted among all the experiments and condition tested. These results, together with $(h\text{-}y_1)/\lambda$ and the *Ir* number, were compared as a function of the dispersion parameter, *kh*, having as a result a universal relationship between them. Therefore, these results clearly demonstrated the successful design of this extinction system that could be adapted to achieve the highest energy dissipation depending on the type of wave generated.

This study will continue analyzing the influence of the porosity in the surface of the self-design extinction system. In addition, the numerical model will be used in future experiments to determine the reflection in breakwaters containing an OWC.

CRediT authorship contribution statement

U. Izquierdo: Calibration of the resistive-type wave probes and the wave generation system, Conceptualization, extinction system design, Methodology, experimental campaign, data treatment, Supervision, Writing – original draft. **L. Galera-Calero:** CFD model, experimental campaign, Validation. **I. Albaina:** extinction system design, LABVIEW program, Delta-ASDA software, configuration of the resistive-type wave probes and experimental campaign. **A. Vázquez:** experimental campaign, Validation. **G.A. Esteban:** Conceptualization, extinction system design, CFD model, Writing – review & editing. **J.M. Blanco:** Conceptualization, extinction system design, Writing – review & editing, Supervision.

Declaration of competing interest

The authors declare that they have no known competing financial interests or personal relationships that could have appeared to influence the work reported in this paper.

Acknowledgements

The authors would like also to express their gratitude for the support provided by the Research Groups of the UPV/EHU (GIU19/029) and the Basque Government (IT1314-19), as well as the support provided by the Joint Research Laboratory on Offshore Renewable Energy (JRL-ORE) and the Open Access funding provided by University of Basque Country.

References

Altomare, C., Domínguez, J.M., Crespo, A.J.C., González-Cao, J., Suzuki, T., Gómez-Gesteira, M., Troch, P., 2017. Long-crested wave generation and absorption for SPH-based DualSPHysics model. Coast. Eng. 127, 37–54. https://doi.org/10.1016/J.COASTALENG.2017.06.004.

Battjes, J.A., 1974. Surf similarity. In: 14th International Conference of Coastal Engineering, pp. 466–480.

Bruinsma, N., Paulsen, B.T., Jacobsen, N.G., 2018. Validation and application of a fully nonlinear numerical wave tank for simulating floating offshore wind turbines. Ocean Eng. 147, 647–658. https://doi.org/10.1016/j.oceaneng.2017.09.054.

Dalrymple, R.A., Rogers, B.D., 2006. Numerical Modeling of Water Waves with the SPH Method 53, pp. 141–147. https://doi.org/10.1016/j.coastaleng.2005.10.004.

Díaz-carrasco, P., Moragues, M.V., Clavero, M., Losada, M.Á., 2020. 2D water-wave interaction with permeable and impermeable slopes: dimensional analysis and experimental overview. Coast. Eng. 103682. https://doi.org/10.1016/j.coastaleng.2020.103682.

Edinburgh Designs Ltd, 2016. Edinburgh designs [WWW document], 1.9.21. http://www4.edesign.co.uk/.

Electronics, D., 2019. Delta electronics [WWW document]. URL. http://www.deltaww.com/services/DownloadCenter2.aspx?secID=8&pid=2&tid=0&CID=06&itemID=060201&typeID=1&downloadID=ASDA-A2,&title=ASDA-A2&dataType=8;&check=1&hl=en-US, 5.6.21).

Esteban Alcalá, G.A., Vázquez Clemente, A., Albaina López de Armentia, I., Izquierdo Ereño, U., Peña Bandres, A., Blanco Ilzarbe, J.M., Bidaguren Diego, I., 2020. Estudio experimental de La reflexión en un sistema parabólico de disipación de oleaje para un tanque de olas 2D. Dyna Energ. Y Sostenibilidad 9, 1–11. https://doi.org/10.6036/es9877.

Frigaard, P., Brorsen, M., 1995. A time-domain method for separating incident and reflected irregular waves. Coast. Eng. 24, 205–215.

Galera-Calero, L., Blanco, J.M., Izquierdo, U., Esteban, G.A., 2020. Performance assessment of three turbulence models validated through an experimental wave flume under different scenarios of wave generation. J. Mar. Sci. Eng. 8 (11), 881. https://doi.org/10.3390/jmse8110881.

Goda, Y., Suzuki, Y., 1976. Chapter 48 Estimation of incident and reflected waves in random wave experiments. Coast. Eng. Proc. 1 (15), 47. https://doi.org/10.9753/icce.v15.47.

Gómez-Gesteira, M., Cerqueiro, D., Crespo, C., Dalrymple, R.A., 2005. Green water overtopping analyzed with a SPH model. Ocean Eng. 32, 223–238. https://doi.org/10.1016/j.oceaneng.2004.08.003.

Guide, U., 2015. STAR-CCM + ® Documentation.

Higuera, P., Losada, I.J., Lara, J.L., 2015. Three-dimensional numerical wave generation with moving boundaries. Coast. Eng. 101, 35–47. https://doi.org/10.1016/j.coastaleng.2015.04.003.

Hirt, C.W., Nichols, B.D., 1981. Volume of fluid (VOF) method for the dynamics of free boundaries. J. Comput. Phys. 39, 201–225. https://doi.org/10.1016/0021-9991(81)90145-5.

Hodaei, S.M.R., Chamani, M.R., Moghim, M.N., Mansoorzadeh, S., Kabiri-Samani, A., 2016. Experimental study on reflection coefficient of curved perforated plate. J. Mar. Sci. Appl. 15, 382–387. https://doi.org/10.1007/s11804-016-1383-5.

Hughes, S.A., 1993. In: Advanced, S. (Ed.), Physical Models and Laboratory Techniques in Coastal Engineering. World Scientific Publishing Co., Singapore.

Iribarren, R., Nogales, C., 1949. Protection des Ports. In: XVII International Navigation Congress.

Isaacson, M., 1991. Measurement of regular wave reflection. J. Waterw. Port, Coast. Ocean Eng. 117, 553–569.

Ish, S.N.M., Raju, P.V.P., 2004. Wave interaction with parabolic corrugated and perforated wave absorbers. J. Hydraul. Eng. 37–41. https://doi.org/10.1080/09715010.2004.10514741.

Izquierdo, U., Galera-Calero, L., Albaina, I., Esteban, G.A., Aristondo, A., J.M.B, 2019. Experimental and Numerical Characterisation of a 2D Wave Flume. DYNA. https://doi.org/10.6036/9244.

Izquierdo, U., Esteban, G.A., Blanco, J.M., Albaina, I., Peña, A., 2019a. Experimental validation of a CFD model using a narrow wave flume. Appl. Ocean Res. 86, 1–12. https://doi.org/10.1016/j.apor.2019.02.012.

Izquierdo, U., Galera-calero, L., Albaina, I., Esteban, G.A., Aristondo, A., Blanco, J.M., 2019b. Experimental and numerical characterisation of a 2D wave flume. Caracterización experimental y numérica de un tanque de olas en 2D. Dyna 94, 662–668. https://doi.org/10.6036/9244.

Lim, H., 2014. Optimum design of a sloping-wall-type wave absorber placed in a sinusoidal propagating wave. Ocean Eng. 88, 588–597. https://doi.org/10.1016/j.oceaneng.2014.03.029.

López, I., Pereiras, B., Castro, F., Iglesias, G., 2014. Optimisation of turbine-induced damping for an OWC wave energy converter using a RANS – VOF numerical model. Appl. Energy 127, 105–114. https://doi.org/10.1016/j.apenergy.2014.04.020.

Machado, F.M.M., Lopes, A.M.G., Ferreira, A.D., 2018. Numerical simulation of regular waves: optimization of a numerical wave tank. Ocean Eng. 170, 89–99. https://doi.org/10.1016/j.oceaneng.2018.10.002.

Madsen, P.A., 1983. Wave Reflection from a vertical permeable wave absorber. Coast. Eng. 7, 381–396.

Mansard, E.P.D., Funke, E.R., 1980. The measurement of incident and reflected spectra using a least squares method. 17th Int. Conf. Coast. Eng. 154–172.

MathWorks, MATLAB.

Mora, A., Bautista, E., Méndez, F., Barbosa, M., 2018. Asymptotic solution for the reflection of long water waves by asymmetric convergent/divergent harbours. J. Coast Res. 34, 383–399. https://doi.org/10.2112/JCOASTRES-D-16-00224.1.

National Instruments, 2016. LabVIEW 2016 (64-bit) - English.

Ouellet, Y., Datta, I., 1986. A survey of wave absorbers Revue des amortisseurs à houle. J. Hydraul. Res. 24, 265–280. https://doi.org/10.1080/00221688609499305.

Puspita, A.I.D., Pallu, M.S., Thaha, M.A., Maricar, F., 2019. Study of reflection and transmission coefficients of waves from perforated plates and introducing dimensionless parameter θ. Earth Environ. Sci. https://doi.org/10.1088/1755-1315/419/1/012135.

Puspita, A.I.D., Pallu, M.S., Thaha, M.A., Maricar, F., 2020. The effect of wave reflection coefficient to the breaker parameter on OWEC breakwater. IOP Conf. Ser. Earth Environ. Sci. 419 https://doi.org/10.1088/1755-1315/419/1/012135.

Tiedeman, S., Allsop, W., Russo, V., Brown, A., 2012. A demountable wave absorber for wave flumes and basins. Coast. Eng. Proc. 1, 1–10. https://doi.org/10.9753/icce.v33.waves.37.

Tutar, M., Veci, I., 2016. Performance analysis of a horizontal axis 3-bladed Savonius type wave turbine in an experimental wave flume (EWF). Renew. Energy 86, 8–25. https://doi.org/10.1016/j.renene.2015.07.079.

Viviano, A., Naty, S., Foti, E., 2018. Scale effects in physical modelling of a generalized OWC. Ocean Eng. 162, 248–258. https://doi.org/10.1016/j.oceaneng.2018.05.019.

Windt, C., Davidson, J., Ringwood, J.V., 2018. High- fidelity numerical modelling of ocean wave energy systems: a review of computational fluid dynamics-based numerical wave tanks. Renew. Sustain. Energy Rev. 93, 610–630. https://doi.org/10.1016/j.rser.2018.05.020.

Xie, N., Hann, M., Pemberton, R., Iglesias, G., Greaves, D., 2019. A numerical and experimental investigation of the effect of side walls on hydrodynamic model testing in a wave flume. Ocean Eng. 186, 106108 https://doi.org/10.1016/j.oceaneng.2019.06.013.

Zhao, X., Hu, C., 2012. Numerical and experimental study on a 2-D floating body under extreme wave conditions. Appl. Ocean Res. 35, 1–13. https://doi.org/10.1016/j.apor.2012.01.001.

Zhao, X.L., Ning, D.Z., Liang, D.F., 2019. Experimental investigation on hydrodynamic performance of a breakwater-integrated WEC system. Ocean Eng. 171, 25–32. https://doi.org/10.1016/j.oceaneng.2018.10.036.